Water Research 295 (2026) 125556

Contents lists available at ScienceDirect

Water Research

journal homepage: www.elsevier.com/locate/watres

Organic colloid composition in variable-redox porewaters within a mountainous floodplain

Brandy D. Stewart [a], Sharon E. Bone [a,b,*], Eleanor Spielman-Sun [a], Matthew A. Marcus [c], Samuel Pierce [d], Kristin Boye [a], Vincent Noël [a]

[a] Stanford Synchrotron Radiation Lightsource, SLAC National Accelerator Laboratory, Menlo Park, CA, 94025, USA
[b] Institute of Bio- and Geosciences, IBG-3:Agrosphere, Forschungszentrum Juelich, 52428, Germany
[c] Advanced Light Source, Lawrence Berkeley National Laboratory, Berkeley, CA 94720, USA
[d] Department of Earth System Science, Stanford University, Stanford, CA, 94305, USA

HIGHLIGHTS

- Riparian colloids show variable organic composition as a function of redox.
- Carboxylate-rich organic matter embedded with Fe(II)/Fe(III)-rich phases.
- Burial of young, organic rich layer of sediment provides microbially available carbon.
- Reducing conditions mobilize iron- and carboxylate-rich organic colloids.

GRAPHICAL ABSTRACT

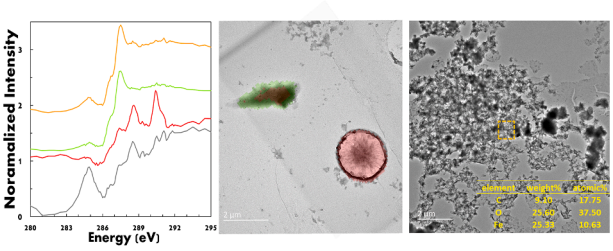

ARTICLE INFO

Keywords:
Scanning transmission X-ray microscopy
Transmission electron microscopy
Alpine floodplain
Organic matter

ABSTRACT

Redox gradients, often driven by changes in sediment moisture levels in porous, heterogeneous groundwater systems, create dynamic conditions that may promote the production and transport of colloids within natural waters. While much research has focused on the inorganic composition of colloids, the organic composition remains less well understood. Organic matter (OM) in colloids may associate with minerals, complex metal ions, and serve as an electron donor for microbial respiration; therefore, its composition is of high interest. We examined the composition of porewater OM along a redox gradient in a riparian soil located along the Slate River in Crested Butte, Colorado, USA as a function of depth (90, 130, 200, and 350 cm below ground surface). All depths were oxic to suboxic, except 200 cm, where the products of iron and sulfate reduction were observed concomitant with an increase in dissolved and/or colloidal OM, pH, alkalinity, and conductivity. We investigated the composition of porewater using correlated scanning transmission X-ray microscopy and transmission electron microscopy. We observed a change in the OM chemistry from carboxylate-rich at the 200 cm depth (where it was also enmeshed with non-crystalline iron) to phenol- and substituted-aromatic-rich at other depths. Radiocarbon dating revealed carbon in porewater at 200 cm was younger than depths above and below. Soil porewater can flow down into the underlaying gravel bed during baseflow conditions, thus we speculate whether riparian porewater could transport iron- and carboxylate-rich organic colloids into surrounding surface waters through the gravel bed conduit.

* Corresponding author at: Institute of Bio- and Geosciences, IBG-3:Agrosphere, Forschungszentrum Juelich, 52428, Germany.
E-mail address: s.bone@fz-juelich.de (S.E. Bone).

https://doi.org/10.1016/j.watres.2026.125556
Received 10 November 2025; Received in revised form 7 February 2026; Accepted 10 February 2026
Available online 12 February 2026

1. Introduction

Floodplains play a pivotal role in regulating the quality and quantity of water delivered to rivers and aquifers (Harvey and Gooseff, 2015; Opperman et al., 2013; Wohl et al., 2018). As zones of frequent hydrological exchange and thus steep redox gradients, they promote the formation and transport of dissolved constituents and colloids (1nm–1 μm) (Lair et al., 2009; Noël et al., 2017; Spielman-Sun et al., 2024). Owing to their high specific surface area and density of reactive surface sites, colloids are key carriers of critical substances, including organics, nutrients, heavy metals, and pollutants (Dia et al., 2000; Flury and Qiu, 2008; Kretzschmar and Sticher, 1998; Löv et al., 2018; Means and Wuayaratne, 1982; Pédrot et al., 2008; Pontoni et al., 2016; Said-Pullicino et al., 2021). While significant research has been devoted to characterizing mineral colloids, the organic fraction of colloids remains poorly understood (Spielman-Sun et al., 2024). Yet recent evidence suggests that organic matter (OM) commonly dominates the mass, controls the surface reactivity, and stabilizes the structure of mixed organic-inorganic colloids, profoundly impacting colloid stability, reactivity, and transport (Dibbern et al., 2014; Lehmann et al., 2021). Colloids can be mobilized by changes in pH and ionic strength, as these modify particle charge and the ability for materials to adsorb and aggregate. Dissolution and precipitation of mineral phases can also result in colloid formation (Nierop et al., 2002; Buettner et al., 2014). Field and laboratory studies have shown that both anoxic (Babey et al., 2022; Giannetta et al., 2022) and oxic (Lyvén et al., 2003; Nierop et al., 2002) conditions can trigger the formation and/or release of organic-rich colloids, enhancing the mobility of C and trace elements in floodplain environments (Said-Pullicino et al., 2021). As the generation of organic-rich colloids is tightly coupled to redox-driven shifts in pH, ionic strength, and mineral solubility, redox cycling must be considered when evaluating floodplain solute exports (Thompson et al., 2006; Buettner et al., 2014; Bunn et al., 2002). Despite this growing recognition, detailed characterization of the organic composition across the dissolved–colloidal continuum is still lacking, particularly in floodplain sediments subject to redox variability (Riedel et al., 2013).

Understanding the speciation of mobilized carbon in floodplain porewaters is critical for predicting how OM interacts with minerals and trace metals and supports microbial processes (Afsar et al., 2020). OM may adsorb to, coprecipitate with, and structurally stabilize nano-minerals, thereby extending colloid lifetimes and influencing the fate of metals (Baalousha, 2009; Liao et al., 2020; ThomasArrigo et al., 2019; Zhou et al., 2018). Our previous research demonstrates that high organic or Si loadings can passivate ferrihydrite nanoparticles, preserving Fe(III) in environments where bulk mineral phases would otherwise transform, a phenomenon sometimes described as the "protective role" of C (Engel et al., 2023). Additionally, colloidal OM serves as an electron donor for microbial respiration (Pédrot et al., 2011), fuels reductive dissolution of Fe-(oxyhydr)oxides (Amirbahman et al., 1997; Pan et al., 2024), and modulates redox buffering capacity in aquifers and hyporheic zones (Yu et al., 2021). Furthermore, colloid-facilitated transport of OM from organic-rich zones to organic-poor gravel beds or surface waters could redistribute carbon within and beyond the floodplain, leading to the propagation of reducing conditions (Aeppli et al., 2022; Babey et al., 2022). Finally, previous studies have shown that redox conditions can influence the composition of organic C: C with a lower nominal oxidation state can be thermodynamically preserved under anaerobic conditions because it does not provide sufficient energy to the microbial cell when coupled with terminal electron acceptors other than oxygen, leading to an increase in the relative abundance of reduced functional groups (e.g. aromatics and aliphatics) or compounds (e.g. lipids or phenol- and aromatic-rich lignin derivatives) under anaerobic compared to aerobic conditions (Boye et al., 2017; Jin and Bethke, 2007; Keiluweit et al., 2017). Despite these implications, the chemical nature and variability of mobilized organic colloids in floodplains, critical to predicting their role in the transport and transformation of C and associated elements, remains poorly understood (Perzan et al., 2021).

This knowledge gap is particularly pressing in mountainous watersheds, often called the "water towers of the world" (Viviroli and Weingartner, 2004), where gravel-bed river floodplains moderate exchanges between snowmelt-fed streams and shallow aquifers (Hauer et al., 2016; Käser and Hunkeler, 2016; Miller et al., 2016). These systems consist of a highly conductive gravel bed capped by a finer-grained, organic-rich soil that acts as a biogeochemical reactor (Hauer et al., 2016; Stanford and Ward, 1993). Hydrologic transitions—snowmelt, beaver-pond inundation, and late-season baseflow—modulate vertical connectivity between the reactive soil and the underlying gravel, thereby controlling delivery of solutes and particles to the aquifer (Wang et al., 2018; Ward et al., 2016). A recent conceptual model, which describes the vertical exchanges between heterogeneous sediment layers typical of alluvial floodplains, illustrates how small changes in inundation area or flow-path geometry may either dilute or concentrate soil-derived constituents in the gravel bed (Babey et al., 2024). Field measurements at the Slate River floodplain (Crested Butte, Colorado) show that anoxic soil water rich in Fe, Mn, and dissolved OM (Dewey et al., 2021; Engel et al., 2023) may be flushed downward via gravel bed underflow during flooding events such as beaver ponding. Contrastingly, under snowmelt conditions the floodplain becomes waterlogged, and the groundwater table pushes upwards from below the soil profile, leading to diminished vertical flow that can oscillate between downwards and upwards (Babey et al., 2024). This leads to diminished impact of the overlying soil on gravel bed biogeochemistry and from surface oxic layers on the anoxic zone.

What remains unknown is the chemical characterization of the organic colloids that accompany these pulses, and whether they retain their identity—and associated metals—during transit through redox-variable porewaters. Here we address this knowledge gap by characterizing the organic colloid composition (<0.6 μm) along a depth-resolved redox gradient in the Slate River floodplain. Using correlated scanning transmission X-ray microscopy (STXM) and transmission electron microscopy (TEM), we probe the molecular fingerprints of OM in the dissolved-colloidal continuum and its associations with non-crystalline Fe phases. By coupling these observations to geochemical profiles, we test the hypothesis that redox transitions dictate not only the abundance but also the functional chemistry (carboxylate- versus aromatic-rich) of mobilized organic colloids. Our findings provide new constraints on how organic-mineral colloids are generated, preserved, and transported in mountain floodplains, with implications for predicting C and metal exports from these critical water-supply basins.

2. Materials and methods

2.1. Site description and field sample collection

Sediment porewater samples (90 cm, 130 cm, and 200 cm depth bgs) were extracted from a previously installed 0.6-μm pore size rhizon nest (19.60.21F, Rhizosphere Research Products) (OBJ1) (Babey et al., 2024) in a floodplain along the upper Slate River (Crested Butte, CO, 38° 54′34.59″ N, 107° 1′43.40″ W) in May, June, and August 2023 and in May 2024. Based on Babey et al., 2024, we expected to find a gradient from oxic-anoxic within the riparian soil for the duration of the sampling season (from May to August); however, we note that downward vertical flow is typically greater under late-season, baseflow conditions (August) than early-season snowmelt conditions (May). The water table is also highest during the spring snowmelt season and lowest in the fall, varying from approximately 35 cm to 105 cm below ground surface (Dewey et al., 2021; Babey et al., 2024). Gravel aquifer groundwater samples (350 cm bgs) were extracted using a Geotech peristaltic pump from a previously installed stainless steel piezometer (Babey et al., 2024) and were immediately filtered through a rhizon identical to those used to extract sediment pore waters to ensure size-fraction consistency across the vertical domain. Aqueous phase chemistry measurements and

sample stabilization for advanced characterization were performed within 5 days of samples reaching the laboratory. Prepared samples were then stored inside a glovebag until analysis. Dissolved oxygen, alkalinity, pH, and aqueous Fe(II) were measured as described in the Supporting Information (SI). Samples were handled anoxically (see SI). A detailed description of the field site setting is provided in Babey et al., 2024.

2.2. Geochemical measurements

Samples were diluted and acidified with 0.5 M trace metal grade nitric acid prior to total metal concentration measurement via inductively coupled plasma-mass spectrometry ICP-MS (Thermo iCAP RQ) and inductively coupled plasma optical emission spectroscopy ICP-OES (Thermo iCAP 6300). Sulfate was measured by ion chromatography IC (Dionex ICS 6000). Samples were diluted with OM-free MQ (18.2 MΩ) water prior to measuring total organic carbon (TOC) and total carbon (TC) on a dissolved organic carbon analyzer (Shimadzu TOC-L). Data were collected in the Environmental Measurements Facility, Stanford University.

2.3. Scanning transmission X-ray microscopy

Porewater samples from 90, 130, 200, and 250 cm depths, May 2024, were prepared for scanning transmission X-ray microscopy (STXM) and transmission electron microscopy (TEM) analyses by drop-depositing 20 μL of sample onto 50-nm thick silicon nitride TEM window arrays (3 mm frame size, containing nine individual 0.1 mm x 0.1 mm windows; Norcada) in an anoxic glovebag. Samples were allowed to dry before being sealed in a mylar bag until analysis. The 3 × 3 square frames allowed for location identification when samples were moved between STXM and TEM. Porewater samples from 200 cm, August 2023 were prepared similarly, using 50-nm thick silicon nitride STXM windows (Norcada) not compatible with TEM. STXM was performed at beamline 5.3.2.2 at the Advanced Light Source (ALS) in a He-filled sample chamber. Samples were transported in a sealed mylar bag and open to the atmosphere only long enough (<2 min) to mount them inside the microscope (chamber was purging with Ar during sample mounting) before pumping the chamber and backfilling with He to maintain anoxic conditions throughout data collection. The Rydberg transition of gaseous CO_2 at 292.74 eV was used for energy calibration at the C 1*s* edge (Prince et al., 1999).

STXM (and TEM) provides the advantage that the chemistry of individual particles can be studied directly (Engel et al., 2023). Although STXM (and TEM) is a microscopic method with an inherently small field of view, the scalability of STXM measurements to bulk observations has been previously documented (Dynes et al., 2015). To ensure we captured sample heterogeneity, we started by scanning the entire STXM window at low resolution to identify where material was present. We then scanned for regions containing C by collecting large, coarse (0.4 μm step size) maps above and below the C K-edge (290 and 280 eV, respectively). We collected maps in regions of ~50 × 50 square microns at three energies across the C K-edge (280, 288.2, 290.3 eV, 0.2 μm step size) and three energies across the Fe LIII-edge (705, 708.5, 710.2 eV, 0.2 μm step size) in order to co-locate organic C, Fe(III), and Fe(II) (Bone et al., 2017; Dynes et al., 2006b). We down-selected smaller regions for detailed analysis of carbon composition via stack maps, in which C K-edge XAS (X-ray absorption spectra) were obtained for each pixel (selected regions typically exhibited optical density (OD) < 2; see below). A single region was studied for each of the 90 and 350 cm depth samples because the abundance of organic carbon-bearing particles was low (the only organic carbon-rich particulate region identified on each sample was measured). For the 130 and 200 cm depth samples, four C-bearing regions were selected based on the following strategy. Firstly, any region in the sample grid that contained material was initially surveyed for co-location of C and Fe. Approximately 70 % of the sample material was surveyed. Regions with C and Fe co-located were selected for analysis followed by areas with distinct morphology. Stack maps were measured until we no longer saw distinct spectra in additional regions. Moreover, we measured one depth (200 cm) from two different years and observed convergent C speciation.

Images were converted to OD by normalization to the incident flux (I_0). All STXM data processing and analysis were performed using STXM image reader (Marcus, 2023) and Athena (Ravel and Newville, 2005). Carbon stack maps were analyzed using principal component and *k*-means cluster analysis (PCA and CA, respectively) (Bone et al., 2017) to extract representative spectra from each stack map. The number of PCA components was selected by examining individual PCA components and selecting all components that were not simply noise around the zero line. This was cross-referenced with the minimum eigenvalue associated with the components. The number of clusters was determined by increasing the number of clusters incrementally (beginning with 2) while simultaneously examining the spectra associated with each cluster. If increasing the numbers of clusters generated either or both i) a distinct spectrum not yet identified in that particular stack map or ii) a noticeable increase in the quality of one or more spectra in the stack map, then the number of clusters was increased. Carbon functional groups were identified in representative spectra based on the peak positions (identified through visual inspection) in comparison to literature-reported values. Additionally, we performed Gaussian fitting to extract the ratio of carboxylate to all more reduced functional groups across samples (details in SI). Some spectra were excluded from Gaussian fitting because they exhibited an intensity dip in the normalized spectra at ~283 eV, which is an artifact of normalization of spectra with low carbon content and transmission signal due to the presence of inorganic material in the sample (Covelli, 2007; Watts et al., 2022). Normalization artifacts impact the relative intensity of features across the entire energy range (Watts et al., 2022); thus, we refrain from attempting semi-quantitative analysis of spectra exhibiting this obvious distortion. Spectra that were excluded were clusters 130–69, 130–59, 200–02, 200–62, and the carbonate-rich spectrum from 350 cm.

Finally, we note that beam damage is not expected under the experimental conditions (Dynes et al., 2006a). We conducted a test in which we collected C XAS data twice in succession on a small region. There were no significant changes in the intensity of the different functional groups, with the exception of the aromatic feature, which gained intensity during the second measurement (Figure S1), consistent with carbon photodeposition within the instrument (Behyan et al., 2011; Watts et al., 2018). Nonetheless, the ratio of carboxylate:reduced functional groups were not significantly impacted by the increased aromatic content (Figure S1). We therefore conclude that no significant alterations to the spectra were observed.

2.4. Transmission electron microscopy and energy dispersive spectroscopy

TEM images and Energy-dispersive X-ray spectroscopy (EDS) data were collected on an FEI Titan Environmental Transmission Electron Microscope equipped with an Oxford Xmax SDD detector and operated at 300 kV at the Stanford Nano Shared Facilities. Images were collected with a Gatan OneView camera. Samples were analyzed with STXM prior to TEM to avoid any alteration to C chemical speciation by TEM, as described in Section 2.3. To ensure TEM analysis was performed in the same position as the STXM measurements the square of interest was first located and then the region measured on STXM was located based on the presence of distinctly shaped particles. A faint mark due to photodeposition during the collection of stack maps (see Section 2.3 above) was also visible and highlighted the previously analyzed region. The direct observation of the presence or absence of lattice features in high-resolution TEM images (~1 nm spatial resolution, approximately 500,000x magnification) was systematically used to discriminate between amorphous or crystalline forms for each particle at each depth (Kogure, 2013).

2.5. Radioactive carbon dating

Radiocarbon dating measurements on porewater and sediment samples were performed at the National Ocean Sciences Accelerator Mass Spectrometry Facility (NOSAMS) at Woods Hole Oceanographic Institution. Porewater samples from May 2024 at all depths were measured in addition to previously collected sediment samples from the same well profile. Sediment samples were first acidified with 1.2 M HCl to remove any inorganic carbon (NOSAMS, 2023A) prior to being combusted via closed-tube combustion in a quartz tube in the presence of copper oxide to ensure complete conversion to CO_2 (NOSAMS 2023B). Finally, CO_2 was graphitized (converted to solid C) using a modified Vogel reduction method (Vogel et al., 1984) to produce graphite with pure hydrogen gas and iron (NOSAMS 2023C). Similarly, porewater samples underwent UV oxidation of carbon to CO_2 prior to being graphitized (Xu et al., 2021). Graphite was then analyzed by accelerator mass spectrometry along with primary and secondary standards and process blanks using a modified National Electrostatics Corporation MC-SNICS ion source, a bounced injection system, and a National Electrostatics Corporation 500 kV pelletron accelerator. Additional details on methodology are described at NOSAMS website (https://www2.whoi.edu/site/nosams/) under the "Sample Preparation Protocols" heading.

3. Results

3.1. Porewater geochemistry

Fig. 1 shows results from geochemical measurements of porewater as a function of depth for May 2024. As depicted in Fig. 1A, the OBJ1 riparian sediment profile is approximately 270 cm deep underlain by gravel. Samples were collected from rhizons at 90, 130, and 200 cm below ground surface (bgs) (riparian soil) and from a piezometer at 350 cm bgs (gravel layer). The pH increased from ~6 in the upper depths to ~6.8 at 200 cm and below. Dissolved oxygen followed an inverse trend with levels initially decreasing as a function of depth from ~3 mg/L at 90 cm to close to 0 at 130 and 200 cm, before increasing to a maximum value of 5 mg/L in the gravel layer (350 cm), indicating the presence of an anoxic region at approximately 200 cm bgs. Consistently, the Fe(II) concentration (a primary indicator of redox state) was highest at 200 cm (80 mg/L) while sulfate was undetectable at this depth. We note, too, that the Mn concentration increased from 90 cm to 200 cm (before decreasing again at 350 cm), which is consistent with the occurrence of an anoxic region at depth in the riparian soil (Table S2). However, the Mn concentration is ~10x lower than the Fe concentration. Alkalinity and conductance also reached their maximum at 200 cm. Similarly, TC, TOC, and inorganic carbon (IC) values were highest at 200 cm (20, 8 and 12 mg-C/L respectively). The porewater geochemistry data are consistent with anaerobic conditions at depth in the riparian soil (where TOC is also highest) before becoming aerobic again in the gravel bed.

Similar trends in porewater TOC, Fe(II) and sulfate were observed in 2023 (Fig. S2), with the highest TOC and Fe(II) and the lowest sulfate occurring at 200 cm. We note that the concentration of TOC was highest in August (Fig. S2). Spring snowmelt leads to the highest groundwater table in May; over the course of the summer, the water table falls, with baseflow typically occurring in August (Babey et al., 2024).

3.2. Carbon K-edge spectra and speciation combined with TEM and EDS

Porewater C speciation was probed in the riparian soil and gravel bed using STXM. Representative spectra were extracted from all images at each depth using PCA and *k*-means clustering. Following STXM, these regions were analyzed with TEM and EDS to correlate C speciation with morphological features and overall elemental composition of the dried colloids. Combining the chemical sensitivity of STXM with the spatial resolution and elemental composition of TEM-EDS allowed for a simultaneous detailed analysis of C speciation, elemental composition, and particle morphology. Fig. 2 shows an example of this combined STXM-TEM-EDS analysis pipeline. STXM-TEM overlays for all images and depths are presented in the SI (Fig S3–9). It is important to note that drying of the colloids can create artifacts, e.g. aggregation or the precipitation of soluble phases (like $CaSO_4$) that form as the water activity decreases (discussed below).

The features in C K-edge spectra arise predominantly from 1 s → π* transitions. The feature at ~285 eV is associated with C in conjugated double bonds and aromatic rings (Cody et al., 1998). Substituents on the aromatic ring result in features at higher energies. The feature at ~286.5 eV is associated with carbon in the aromatic ring that is double bonded to O (i.e., carbonyl-substituted aromatics) (Hitchcock et al., 1992), although other carbonyl groups can also result in peaks in this region

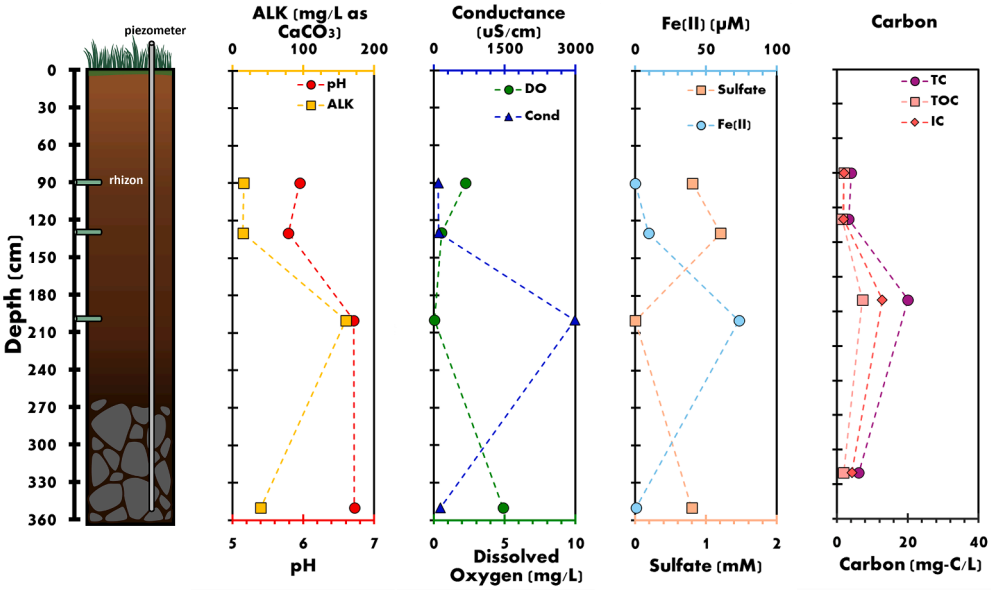

Fig. 1. Schematic of sediment profile showing rhizon and piezometer location (left) and geochemical measurements as a function of depth at OBJ1 (TC = total carbon, TOC = total organic carbon, IC = inorganic carbon).

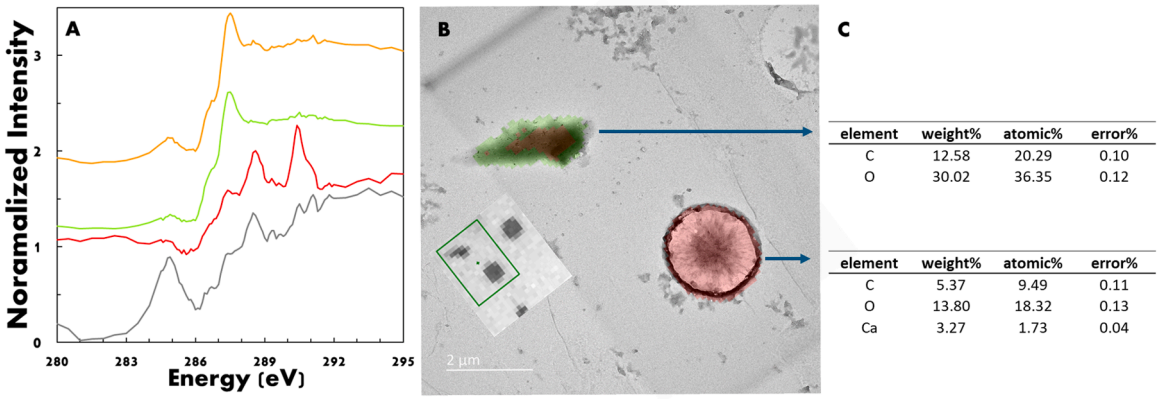

Fig. 2. Carbon K-edge XAS spectra (A), TEM image overlaying *k*-means clusters corresponding to XAS spectra (B), and chemical composition of clusters (C) determined by EDS for 350 cm sample. Inset in (B) shows resolution of STXM image of same region for comparison. Colors in (A) correspond to cluster colors in (B) with gray spectrum generated from background (non-colored) region.

(Wan et al., 2007), which hereafter, is referred to as "substituted aromatics". The feature at ~287.5 eV is associated with C in phenol groups (Wan et al., 2007). Aliphatic C exhibits a 1 s → π*/3p transition at ~287 eV (Hitchcock and Ishii, 1987), which overlaps with phenol, thus we

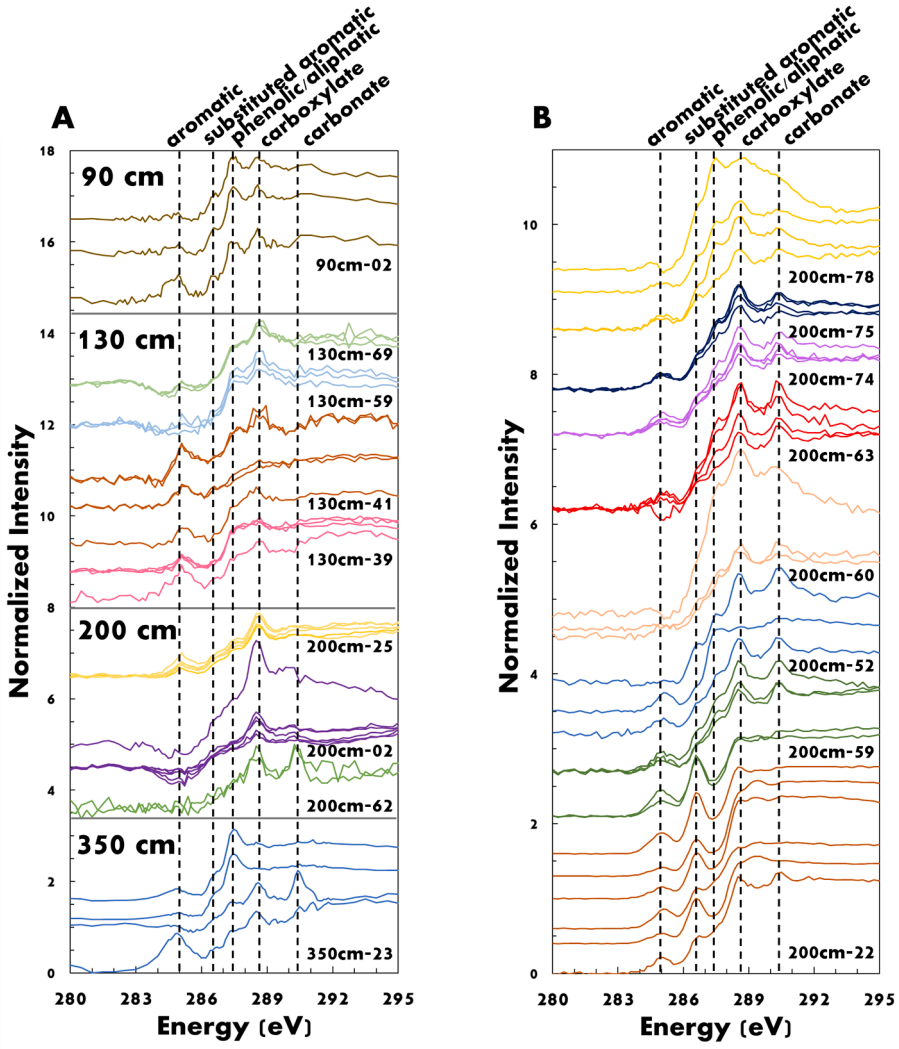

Fig. 3. Carbon K-edge XAS spectra as a function of depth for May 2024 (A) and from 200 cm depth August 2023 (B). Spectra of same color come from cluster analysis of one STXM stack region (denoted by the number following the depth in label).

cannot clearly distinguish the two functional groups, hence this peak is labeled as "phenol/aliphatic". The feature at ~288.5 eV is associated with carboxylate and amide functional groups (Cody et al., 1998; Ishii and Hitchcock, 1988; Benzarara et al., 2004); for brevity these are referred to as carboxylate groups. Below, we discuss the attributes of the representative C spectra along with their association to specific elemental and morphological features as a function of depth (Fig. 3 and S3–9).

Carbon K-edge spectra in the suboxic/oxic, riparian zone soils (90 and 130 cm depths) were characterized by dominant features in the aromatic and phenolic/aliphatic regions, and a carboxylate feature (Fig. 3). At the 90 cm depth a small contribution from alcohol at ~289.3 eV was observed. In many spectra, a pronounced shoulder was also visible in the substituted aromatic region. At 90 cm TEM revealed many "sand dollar" like objects with amorphous material in between (Fig. S10). The sand dollars, which were identified as $CaSO_4$ based on their elemental composition, likely formed upon sample drying (Fig. S3, S6, S7). The C K-edge spectra were associated with the amorphous material, which contained Al and Ca along with C (Fig. S3). Few organic-rich particles were identified in the 90cm sample; instead, C was distributed diffusely across the sample window, with little variation in intensity. This organic material may have been truly dissolved and/or nanoparticles less than the size of the beam (50 nm) distributed sparsely across the STXM window. The sand dollar objects were also present at 130 cm, along with finer features (Fig. S10B), which contained Fe particles enmeshed in carbon (Fig. S7). Finally, one image taken at 130 cm showed amorphous particles with only C present (Fig. S4). We could not identify a trend in C speciation as a function of elemental composition based on comparison of STXM and TEM-EDS images at 90 and 130 cm depths.

In the oxic gravel bed (350 cm), three distinct C spectra were identified, one associated with a "smudge-like" particle (containing C and O), one associated with a sand dollar feature (containing C, O, and Ca), and one associated with the background (Fig. 2). The "smudge-like" particle exhibited large aromatic and phenol/aliphatic features, a small shoulder in the substituted aromatic region, and a small carboxylate feature. The spectrum associated with the sand dollar exhibited phenol and carboxylate peaks and a large feature at ~290.2 eV (characteristic of carbonate; Wan et al., 2007). The final spectrum associated with the background was similar to that associated with the sand dollar, except that it exhibited much less intensity at 290.2 eV and a large feature in the aromatic region. Similar to the 90 cm sample, we identified few organic C-rich particles at this depth and instead much of the carbon appeared as a coating. We interpret the sand dollar particle to be calcium carbonate or sulfate coated with aromatic-rich organic C based on the C K-edge spectra as well as the presence of Ca (Fig. 2). Due to its size, which was larger than the 0.6 μm-filter used to extract the porewater sample, we expect that this mineral particle precipitated or aggregated upon drying.

The C species identified in the oxic depths (90, 130, and 350 cm) were characterized by more reduced organic functional groups (like aromatics, substituted aromatics, and phenols/aliphatics) in comparison to a small contribution from more oxidized organic functional groups (mostly carboxylate) (Fig. 3A). In contrast, the porewater organic matter from the anoxic riparian soil at 200 cm was distinct from the other depths, both in May 2024 and August 2023 (Fig. 3B). The majority of spectra were elevated in carboxylate functional groups, with minor contributions from reduced functional groups and carbonate. These spectra were similar to OM that is microbially derived and mineral-associated, which has been identified in numerous soils via STXM (Keiluweit et al., 2012; Lutfalla et al., 2019; Solomon et al., 2012). Unlike lignin, microbial residues are much higher in carboxylate and amide due to their cellular protein content. Bacterial cells, in fact, exhibit very similar spectra to the spectra of proteins (Keiluweit et al., 2012). In many soil systems, C K-edge spectra exhibit carboxylate/amide as the dominant peak, with smaller features at 285 eV and ~286–287 eV, reflecting the mixture of plant and microbial residues and their breakdown products, similar to what we observe here. We therefore infer that the porewater OM at 200 cm exhibits a higher degree of microbial residues than the porewaters observed at other depths.

In addition to carboxylate-rich C spectra, in August 2023, we also observed a minority of spectra at 200 cm that were dominated by reduced functional groups, especially in the substituted aromatic region (e.g., 200 cm-22 and 200 cm-59 in Fig. 3B). Some of these substituted aromatic-rich spectra also exhibited a small shoulder at lower energies than the aromatic feature, which could correspond to quinone functional groups (~284.4 eV) (Cody et al., 1998) The origin of these spectra is discussed below.

TEM images revealed particles with distinct morphologies at the 200 cm depth (Fig. S10C). The dried aggregates appeared as a web of crumpled sheet-like particles, with elevated C and Fe content and a C/Fe molar ratio of ~7 – 16 (Fig. 4 and S8, 9). Fig. 4 shows an overlay of C, Fe (II), and Fe(III) (obtained via STXM). Fig. 4B shows a TEM image of a portion of the STXM map. The bright yellow features (concentrated Fe regions in Fig. 4A) appear dark in the TEM image likely due to a combination of higher Z value than the surrounding C-rich areas and greater sample thickness. A high-resolution TEM image (Fig. 4C), which was taken in the region noted by the orange square in Fig. 4B, indicates that the Fe(II)-Fe(III)-C mesh is amorphous (as indicated by the absence of lattice fringes). Particles with elevated C and Fe were observed previously at this site: Engel et al. (2023) reported a C/Fe ratio of 12.8 in snowmelt (May) colloids collected at a depth of 180 cm. We interpret our data to show Fe particles enmeshed in C-rich matrices. While we cannot completely exclude the possibility that C and Fe were adventitiously associated in our samples due to aggregation of particles during drying, we note that Engel et al. (2023) previously detected Fe-C complexes via EXAFS at similar depths at this field site.

3.3. C oxidation as function of depth

To semi-quantitatively compare organic material at the 200 cm, anoxic depth to the other (suboxic-oxic) depths, we examined the ratio of carboxylate functional groups (~288.5 eV) to all more reduced functional groups (aromatic, substituted aromatic, and phenolic/aliphatic, from ~284 – 287.5 eV) as a proxy of the average oxidation state of organic C and presence of proteinaceous, microbial residues (Fig. 5A; Gaussian fits shown in SI, Figs. S11-S24). Alcohol was excluded from this analysis because its abundance was highly correlated with the fitted parameters for the background functions (SI, "Gaussian Fitting"), it was present in a minority of spectra, and because it does not serve as an effective proxy of proteinaceous, microbial material. This approach was based on Keiluweit et al., 2017, who used the ratio of carboxylate-C to aromatic-C obtained via C K-edge XAS as a proxy for organic C oxidation state. This ratio serves as a proxy for average oxidation state of C because the oxidation state of carbon increases as the number of O atoms to which it is bound increases (C in carboxylate functional groups is bound to two O atoms, or in the case of amide, one O and one N atom; only inorganic carbon is more oxidized). However, we included substituted aromatic, and phenolic/aliphatic-C in addition to aromatic-C because these types of C are bound to zero or one O atoms (so they are less oxidized than carboxylate-C) and because they were prominent in several of our spectra. The ratio was determined based on the average of the functional group composition of all spectra analyzed at each depth. As expected, based on our qualitative description of the sample spectra provided above, the ratio of carboxylate to reduced functional groups was elevated at 200 cm (0.63 ± 0.05 in May 2024 and 0.69 ± 0.18 in August 2023) relative to the other depths (which ranged from 0.33 ± 0.06 to 0.54 ± 0.17). Thus, it appears that the most reducing conditions in this riparian system harbored the most oxidized organic C with the most proteinaceous, microbial characteristics.

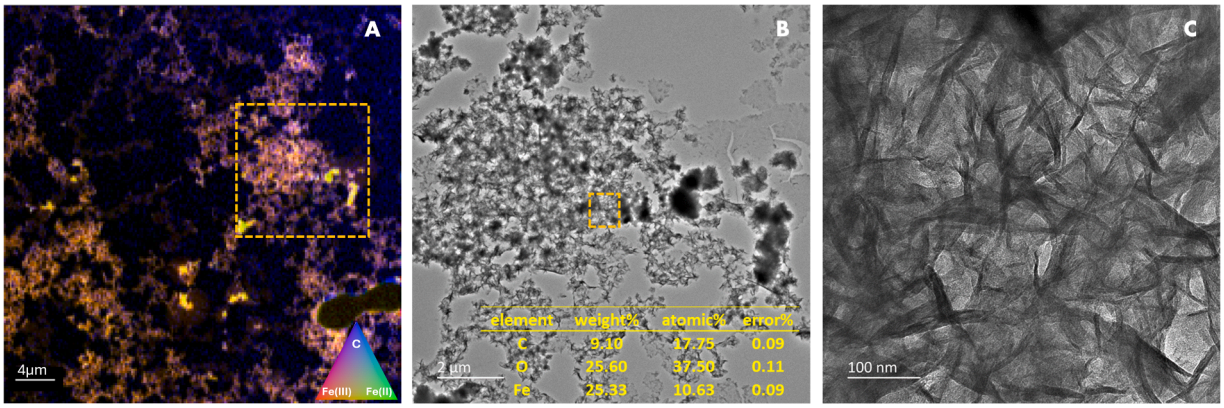

Fig. 4. Combined C and Fe STXM map (A) and TEM images (B, C) of subregions (shown in orange boxes) of 200 cm sample showing C and Fe co-location (A) in an amorphous material (C). In panel A, overlap between C, Fe(III) and Fe(II) is indicated by orange; Ca and Fe(III) by purple; and Fe(II) and Fe(III) by yellow.

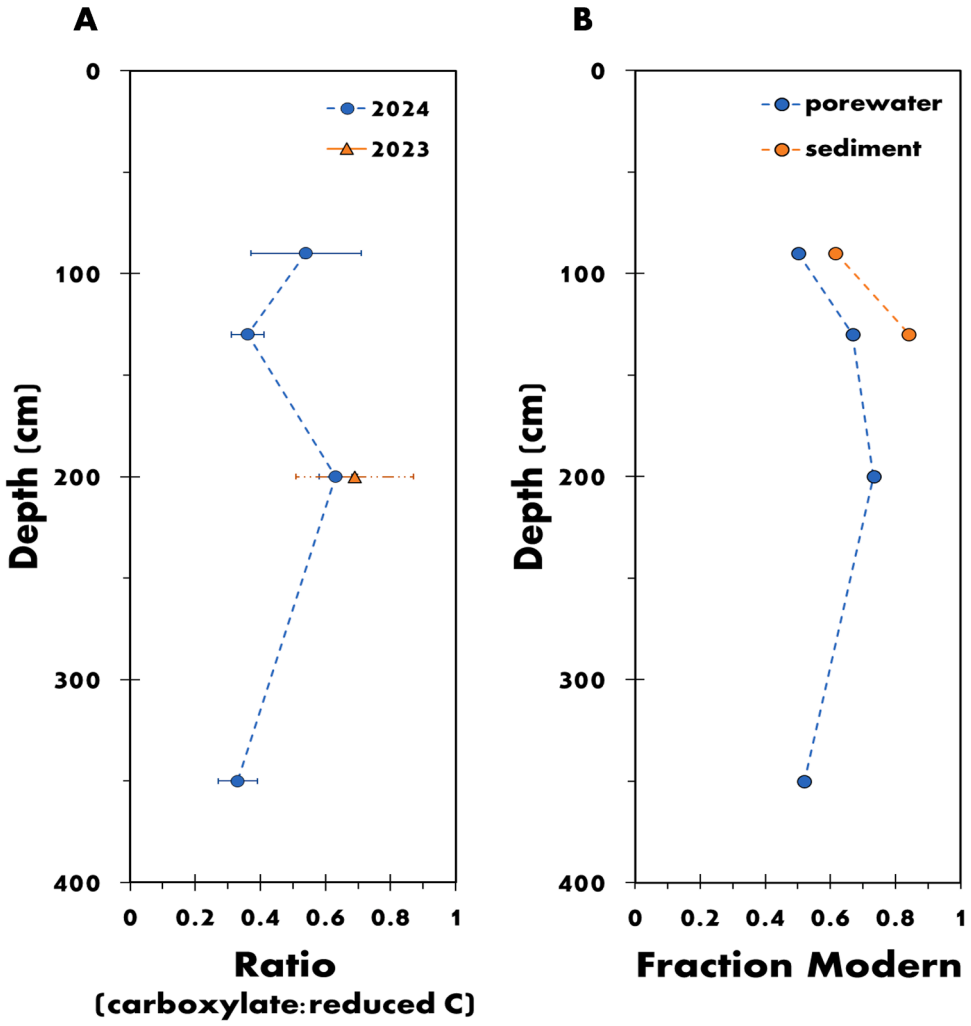

Fig. 5. Ratio of carboxylate/amide carbon to reduced forms of carbon (aromatic, substituted aromatic, phenolic/aliphatic) (A) as a function of sample depth showing a greater amount of oxidized C at 200 cm compared to other depths and fraction modern (FM) as a function of depth (B). Ratios were calculated using Gaussian fitting of C K-edge XANES spectra.

3.4. Sediment and porewater radiocarbon dating

Results from sediment and porewater radiocarbon dating are presented in Table 1 and Fig. 5B (accession numbers OS-186,834-35, 187,435–38). The fraction modern (FM) in porewater varied between 0.500 ± 0.014 at 90 cm and 0.732 ± 0.006 at 200 cm, corresponding to approximate carbon age of 5550 to 2500 years. The youngest carbon was recorded in the 200 cm porewater sample (0.73 FM, 2500 years). Sediment samples from 90 to 130 cm were also measured with FM values 0.620 ± 0.001 and 0.841 ± 0.002 of respectively. Carbon age

Table 1
Results from sediment and porewater radiocarbon dating showing fraction modern (FM), age, and% carbon derived from shale (%C_{shale}) as a function of depth.

sample	FM	Age (yr)	%C_{shale}
90 cm porewater	0.500 ± 0.014	5550 ± 220	49.9
90 cm sediment	0.620 ± 0.001	3900 ± 20	38.5
130 cm porewater	0.668 ± 0.005	3250 ± 65	33.2
130 cm sediment	0.841 ± 0.002	1390 ± 15	15.9
200 cm porewater	0.732 ± 0.006	2500 ± 65	26.8
350 cm porewater	0.520 ± 0.012	5260 ± 190	48.0

followed the same trend in porewater and sediment samples between 90 and 130 cm, where younger material underlay older material.

4. Discussion

4.1. Source of carbon in porewater samples

We observe a trend in both C speciation and age as a function of depth and redox status in the sediment porewaters. Older, more reduced carbon species occurred at the shallowest depth in the riparian soil (90 cm) and in the deepest location in the gravel bed (350 cm) where porewaters were oxic. We observed the youngest and most oxidized C at 200 cm, where porewaters were anoxic and supported Fe(III) and sulfate reduction. Carbon at the 200-cm depth was also distinct in that it co-occurred with Fe, which for one sample was identified as amorphous, mixed Fe(II)-Fe(III) particles. The 130-cm depth in the riparian soil was intermediate, both in terms of porewater chemistry and age (Fig. 5).

The Slate River floodplain examined in our study overlies Mancos shale, which could be the source of old C in the sediments. In the adjacent East River catchment, Fox et al. (2020) argued that organic matter in the floodplain came from shale weathering, which was supported by C-dating of the shale and of soils/sediments collected from the riparian zone, and the similarity between the C K-edge XAS of floodplain sediments and shale outcroppings collected from the same field site. Additionally, Stolze and colleagues used reactive transport modeling to predict shale weathering rates in the hillslope subsurface of East River (Stolze et al., 2023). Based on their model, which included terms for microbial decomposition of plant-derived OM and dissolution of OM from shale, they argued that below approximately 1 m, the soil profile switches from being dominated by modern C to being dominated by shale-derived C. The prevalence of shale-derived C at depth in the hillslope profile, and its abundance (~30 %) in floodplain sediments in the East River suggest the presence of shale in the floodplain sediments at nearby Slate River.

By assuming two endmembers - lignin with an FM of 1 and shale with an FM of 0 – Fox et al. (2020) calculated the % C_{shale} in a sample using the following equation:

$$\%\ C_{shale} = 100(1 - FM)$$

Following the same method we calculated % C_{shale} values for the Slate River samples (Table 1) and found porewater values ranging from 26 % in the 200 cm sample to ~50 % in the 90 and 350 cm porewater samples. The 90 and 130 cm sediment samples had 39 and 16 % C_{shale} respectively. The lowest porewater % C_{shale} occurred in the 200-cm sample where the youngest date and highest FM were measured. This range is in line with Fox et al.'s report of 30 % shale-derived carbon in the nearby East River catchment.

The STXM spectra measured at 90, 130, and 350 cm are consistent with a mixture of shale and lignin (i.e., plant) derived organic carbon. Spectra from Fox et al. (2020) were similar to spectra from our porewaters in the predominance of reduced C species: their shale spectrum exhibited one large, dominant feature in the aromatic region, with shoulders in the quinone and substituted phenolic regions, as well as amplitude from 287–288 eV (phenol and carboxylate) (Fig. S25), while their soil spectra exhibited slightly higher amplitude in the 287–288 eV region, consistent with oxidation during weathering. Comparing our porewater spectra with other published shale spectra, we see that our spectra exhibit similarities with aliphatic and asphaltene extractions, especially in the dominance of features at ~286 and ~287 eV (Bernard et al., 2012). Our spectra were also similar to Bernard et al.'s reference fracture bitumen sample, with the exception that we observed a more pronounced feature in the substituted aromatic region (~286.5 eV). Additionally, several STXM spectra measured at 200 cm in August 2023 (Fig. 3B) showed particles dominated by substituted aromatic rather than carboxylate species, which resembled the asphaltene spectrum reported by Bernard et al. Thus, although the shale spectra from East River (Fig. S24) had no distinct peak corresponding to substituted aromatics, we interpret this as indicating the occurrence of some shale-derived material in the colloidal phase also at 200 cm.

Lignin is a major source of phenols to soil since lignin and its breakdown products are ubiquitous due to its role as a structural component in plants (Huang et al., 2019). The C spectrum of lignin exhibits a large peak in the aromatic region and in the phenolic region, with smaller features at ~286 and ~288 eV (Karunakaran et al., 2015) (Fig. S25). The phenol-rich spectra in our samples differ from lignin in that the aromatic feature is much smaller and the substituted aromatic region is relatively more pronounced. During lignin degradation aromatic/phenolic moieties are oxidized, typically resulting in a decrease in the aromatic and phenolic groups in favor of more oxidized groups, but not in substituted aromatics. We speculate that the OM in riparian soil porewater arises from a combination of lignin degradation products, leading to elevated signal in the phenol region, and weathered shale, which includes high levels of substituted aromatics, consistent with the abundance of these functional groups in our spectra. This interpretation is consistent with the estimated abundance of shale (Table 1).

We measured C speciation and age in porewater samples, whereas Fox et al. (2020) looked only at C in the solid soil matrix of the East River floodplain. Thus, direct comparison between the two studies is limited and dependent on the release and mobility of OM compounds containing different functional groups. Interestingly, Anderson et al. (2023) observed the partitioning of C with low nominal oxidation state and high average molecular weight into water extracts of East River floodplain soils. Unsaturated and condensed hydrocarbons, lignin, and tannin comprised half or more than half of all compounds detected in their water extracts. This suggests that reduced C species, originating from shale or degraded lignin, can be readily mobilized into the aqueous phase, consistent with our observation of such species in porewaters from nearby Slate River riparian soils.

4.2. Influence of redox on carbon speciation in porewaters

The dominance of the most carboxylate-rich, oxidized organic C under the most reducing conditions stands in contrast to prior studies. Barber et al. (2024) examined C speciation in oxic versus anoxic lake sediments via C K-edge XAS. The authors observed that carboxylate dominated in both sediments, but anoxic sediments contained more substituted aromatic and aliphatic/phenol functional groups, in contrast to our observations. Also converse to our findings is the work of Boye et al. (2017) who observed a lower average nominal oxidation state of water extractable organic C in anoxic riparian zone sediments compared to oxic ones. These authors argued that the prevalence of reduced organic C was related to thermodynamic limitation on anaerobic microbial respiration. Finally, we note that Keiluweit et al. (2017) observed more carboxylate-rich, oxidized C in coarse-grained sediments than in fine-grained sediments that exhibited greater anaerobic respiration. We interpret the prevalence of more oxidized C in anoxic porewaters in the Slate River floodplain to arise from the burial and preservation of younger, organic-rich material, consistent with the higher FM content at 200 cm relative to the other depths. This younger, organic-rich layer can support microbial respiration, leading to the

draw-down of O_2 and the onset of reducing conditions. We note, too, that the carbon spectra measured at this depth exhibited features consistent with proteinaceous, microbially derived OM. We cannot unambiguously separate differences in the OM speciation at 200 cm that arise because the organic carbon is younger than the surrounding layers from differences that arise because carboxylate-rich microbial biomass (and necromass) accumulates due to the relatively high concentration of bioavailable OM, which supports iron and sulfate reduction. In fact, prior work at this site identified methanogenic bacteria and archaea, highlighting the prevalence of anaerobic respiratory pathways at anoxic depths (Rasmussen et al., 2024). It would be interesting in future work to measure microbial activity directly and to characterize bacterial groups associated with Fe(III) and sulfate reduction as a function of depth, as these anaerobic respiratory pathways are expected to dominate based on the porewater geochemistry. Such information may help to determine how microbial activity contributes to the OM composition of the porewaters.

The porewaters at 200 cm were also distinguished by the presence of C enmeshed with amorphous Fe(II/III) (Fig. 4). This agrees with prior work by Engel et al. (2023), who observed multiphase OM-Fe-Si assemblages in porewater from the same field site. They identified both poorly crystalline 2-line ferrihydrite coated with OM, as well as complexes of Fe(II) and Fe(III) with OM. The presence of Fe(II) in the Fe-C assemblages in both Engel et al. (2023) and the work presented here are in accordance with our hypothesis described above of increased anaerobic microbial respiration leading to the accumulation of oxidized C and reduced electron acceptors, including Fe(II), in the 200 cm sample relative to the other sample depths. Numerous interactions occur between Fe and C, which can give rise to mixed C-Fe(II)/Fe(III) colloids. The formation of these colloids is therefore likely to be complex, and we can only speculate on the specific chemical mechanisms that give rise to the particles we observed. Beyond chemical associations, reduction of Fe (III) minerals can drive physical changes in the soil matrix as aggregates break apart, which likely influences the form of these colloids (Buettner et al., 2014). It is well-known that Fe(II) can transform Fe(III) mineral phases, although association with (especially) carboxylate-rich C can inhibit transformation (ThomasArrigo et al., 2019). Close Fe and C association can promote cycling of electrons between OM functional groups and Fe, further leading to mixed oxidation state Fe moieties (e.g., Amirbahman et al., 1997). Finally, reactive oxygen species can in some cases be produced by oxygenation of Fe(II)-bearing minerals, which can then oxidize OM (Dong et al., 2023). Thus, there are multiple direct and indirect pathways by which electron transfer between OM and Fe can occur, leading to dynamic redox cycling of Fe and transformation of both Fe and OM.

We posit that seasonal redox variability could play a key role in determining the source and extent of mobilized C in the riparian soil. TOC concentrations in porewater were lower in May 2024 and higher in Augst 2023 at ~200 cm, while Fe(II) was higher in May and lower in August (Fig. S1), consistent with intensified C mobilization under late-season baseflow conditions, which are more oxic. Oxygen promotes degradation of highly reduced shale-derived carbon (Stolze et al., 2023), thermodynamically favoring the mobilization of this C under oxic rather than anoxic conditions. Based on this, we hypothesize that shale-derived C contributes significantly to mobilized C at 200 cm during baseflow (drier) seasons, when oxygen can penetrate to this depth (consistent with the identification of shale-derived C in August 2023, but not May 2024). Thus, we expect C speciation (and concentration) to vary as a function of both depth and season as the redox conditions in the riparian soil shift, although more frequent temporal sampling across season is needed to address this hypothesis. Variability in the chemical composition of colloidal carbon could drive different biogeochemical processes during these redox cycles — for example, by altering electron transfer pathways or by modifying the protective role of OM when associated with mineral nanoparticles (ThomasArrigo et al., 2019). Moreover, vertical downward flow from the riparian soil to the gravel bed occurs under baseflow conditions, such that it is the late-season colloids that may be transported to the river (Babey et al., 2024).

We posit that the preservation of a younger, organic-rich layer of sediment provides a microbially accessible (bioavailable) source of C that stimulates microbial respiration, leading to the draw down of oxygen, the appearance of reduced species (i.e. elevated levels of Fe(II)), and the enrichment of microbially-derived C in porewaters. This promotes the mobilization of C- and Fe(II)/(III)-rich colloids into porewaters. Vertical downward flow can bring material from the riparian soil into the gravel bed below, which is hydrologically connected to the river, providing a vector for C-Fe colloids to the stream, especially when downward vertical flow is greatest during baseflow in the late summer/early fall (Babey et al., 2024; Engel et al., 2023). The coupled colloidal mobilization of Fe and C we observe in the Slate River floodplain has been observed previously in other redox-active floodplains, including in the arid Jemez mountains of New Mexico and in thawing permafrost in the arctic and subarctic, leading to so-called “rusting rivers” due to the orange color of the Fe rich colloids (Buettner et al., 2014; Thompson et al., 2011; Winkler et al., 2018). Our work thus underscores the importance for redox-driven colloidal C-Fe mobilization, especially in dynamic floodplain systems where river migration and beaver dam formation provide mechanisms for burial and preservation of young, organic rich sediments (D’Elia et al., 2017; Dewey et al., 2022).

5. Conclusions

We observed different organic C speciation as a function of depth and redox status in porewaters from riparian zone soils in an alpine catchment. The most oxidized OM was observed at 200 cm, where the highest Fe(II) and the lowest sulfate and oxygen concentrations were also measured, indicating the presence of reducing conditions. Porewaters at this depth were also enriched in OM relative to the other depths and contained the highest fraction of modern C (i.e., youngest C). We argued that the organic C in the anoxic porewaters was associated with Fe and exhibited a more microbial signature than the other depths, which were characterized largely by a mixture of lignin and shale-derived materials. We therefore concluded that the burial of young, organic rich materials provide microbially available C, leading to the draw down of oxygen and the onset of reducing conditions. During late season baseflow conditions, we observed some shale-derived carbon at 200 cm, which may have been mobilized as oxygen penetrates deeper into the riparian soil under drier, late season conditions. Together, these observations suggest that redox cycling in riparian soils can lead to mobilization of C- and Fe-rich colloids, which may be transported to the river.

CRediT authorship contribution statement

Brandy D. Stewart: Writing – review & editing, Writing – original draft, Visualization, Investigation, Formal analysis, Conceptualization. **Sharon E. Bone:** Writing – review & editing, Writing – original draft, Visualization, Project administration, Investigation, Formal analysis, Conceptualization. **Eleanor Spielman-Sun:** Writing – review & editing, Methodology, Investigation. **Matthew A. Marcus:** Writing – review & editing, Methodology, Investigation. **Samuel Pierce:** Writing – review & editing, Investigation. **Kristin Boye:** Writing – review & editing, Project administration, Funding acquisition. **Vincent Noël:** Writing – review & editing, Writing – original draft, Supervision, Project administration, Conceptualization.

Declaration of competing interest

The authors declare that they have no known competing financial interests or personal relationships that could have appeared to influence the work reported in this paper.

Acknowledgements

This work was supported by the Watershed Function Science Focus Area funded by the US Department of Energy, Office of Science, Biological and Environmental Research at SLAC Accelerator National Laboratory under Contract No DE-AC02-76SF00515 and at Lawrence Berkeley National Laboratory under Contract No DE-AC02-05CH1123. STXM data was collected at beamline 5.3.2.2 at the Advanced Light Source, a U.S. DOE Office of Science User Facility under contract no DE-AC02-05CH11231. Transmission electron microscopy (TEM) and EDS measurements were conducted at the Stanford Nano Shared Facilities (SNSF) RRID: SCR_023230, supported by the National Science Foundation under award ECCS-2026822. Radiocarbon dating measurements were performed at the National Ocean Sciences Accelerator Mass Spectrometry Facility (NOSAMS), supported by the National Science Foundation (NSF Cooperative Agreement number, OCE-1755125). We thank Patricia Fox for sharing the shale spectrum with us, Chithra Karunakaran from the Canadian Light Source for sharing the lignin spectrum, Andrew Barnum and Pinaki Mukherjee for guidance with microscopy data collection, Lizzie Paulus for assistance with ICP and TOC measurements, Peter Nico for thoughtful insights on soil carbon, and Dave Daye for manufacturing sample holders. We thank Hans-Georg Steinrueck from Forschngszentrum Juelich for advise regarding python-based Gaussian fitting. We thank Jennie Reithel, Rocky Mountain Biological Laboratory, and the Crested Butte Land Trust for field station support and access to research sites on the Slate River.

Supplementary materials

Supplementary material associated with this article can be found, in the online version, at doi:10.1016/j.watres.2026.125556.

Data availability

The chemical datasets presented in this study can be found in online repositories. NCBI under accession PRJNA626616, ESS-DIVE under doi:10.15485/3016270. Other data available on request.

References

Aeppli, M., Babey, T., Engel, M., Lacroix, E.M., Tolar, B.B., Fendorf, S., Bargar, J.R., Boye, K., 2022. Export of organic carbon from reduced fine-grained zones governs biogeochemical reactivity in a simulated aquifer. Env. Sci. Technol. 56 (4), 2738–2746.

Afsar, M.Z., Goodwin, C., Beebe, T.P., Jaisi, D.P., Jin, Y., 2020. Quantification and molecular characterization of organo-mineral associations as influenced by redox oscillations. Sci. Total Environ. 704, 135454.

Amirbahman, A., Sigg, L., Gunten, U.v., 1997. Reductive dissolution of Fe(III) (Hydr) oxides by cysteine: kinetics and mechanism. J. Colloid. Interface Sci. 194 (1), 194–206.

Anderson, C.G., Goebel, G.M., Tfaily, M.M., Fox, P.M., Nico, P.S., Fendorf, S., Keiluweit, M., 2023. Molecular nature of mineral-organic associations within redox-active mountainous floodplain sediments. ACS Earth Space Chem. 7 (9), 1623–1634.

Baalousha, M., 2009. Aggregation and disaggregation of iron oxide nanoparticles: influence of particle concentration, pH and natural organic matter. Sci. Total Environ. 407 (6), 2093–2101.

Babey, T., Boye, K., Tolar, B., Engel, M., Noël, V., Perzan, Z., Kumar, N., Francis, C.A., Bargar, J.R., Maher, K., 2022. Simulation of anoxic lenses as exporters of reactivity in alluvial aquifer sediments. Geochim. Cosmochim. Acta 334, 119–134.

Babey, T., Perzan, Z., Pierce, S., Rogers, B., Wang, L., Carroll, R.W.H., Bargar, J.R., Boye, K., Maher, K., 2024. Mountainous floodplain connectivity in response to hydrological transitions. Water Resour. Res. 60 (7), e2024WR037162.

Barber, A., Mirzaei, Y., Brandes, J., Joshani, A., Gobeil, C., Gélinas, Y., 2024. Redox conditions influence the chemical composition of iron-associated organic carbon in boreal lake sediments: a synchrotron-based NEXAFS study. Geochim. Cosmochim. Acta 382, 51–60.

Behyan, S., Haines, B., Karanukaran, C., Wang, J., Obst, M., Tyliszczak, T., Urquhart, S. G., 2011. In: McNulty, I., Eyberger, C., Lai, B. (Eds.), Surface Detection in a STXM Microscope. AIP, pp. 184–187.

Benzerara, K., Yoon, T.H., Tyliszczak, T., Constantz, B., Spormann, A.M., Brown Jr, G.E., 2004. Scanning transmission X-ray microscopy study of microbial calcification. Geobiology 2 (4), 249–259.

Bernard, S., Horsfield, B., Schulz, H.-M., Wirth, R., Schreiber, A., Sherwood, N., 2012. Geochemical evolution of organic-rich shales with increasing maturity: a STXM and TEM study of the Posidonia Shale (Lower Toarcian, northern Germany). Mar. Pet. Geol. 31 (1), 70–89.

Bone, S.E., Dynes, J.J., Cliff, J., Bargar, J.R., 2017. Uranium(IV) adsorption by natural organic matter in anoxic sediments. Proc. Natl. Acad. Sci. 114 (4), 711–716.

Boye, K., Noël, V., Tfaily, M.M., Bone, S.E., Williams, K.H., Bargar, John R., Fendorf, S., 2017. Thermodynamically controlled preservation of organic carbon in floodplains. Nat. Geosci. 10 (6), 415–419.

Buettner, S.W., Kramer, M.G., Chadwick, O.A., Thompson, A., 2014. Mobilization of colloidal carbon during iron reduction in basaltic soils. Geoderma 221-222, 139–145.

Bunn, R.A., Magelky, R.D., Ryan, J.N., Elimelech, M., 2002. Mobilization of natural colloids from an iron oxide-coated sand aquifer: effect of pH and ionic strength. Env. Sci. Technol. 36 (3), 314–322.

Cody, G.D., Ade, H., Wirick, S., Mitchell, G.D., Davis, A., 1998. Determination of chemical-structural changes in vitrinite accompanying luminescence alteration using C-NEXAFS analysis. Org. Geochem. 28 (7), 441–455.

Covelli, D.S. 2007. X-ray microscopy of hydrocarbon-clay interactions.

D'Elia, A.H., Liles, G.C., Viers, J.H., Smart, D.R., 2017. Deep carbon storage potential of buried floodplain soils. Sci. Rep. 7 (1), 8181.

Dewey, C., Bargar, J.R., Fendorf, S., 2021. Porewater lead concentrations limited by particulate organic matter coupled with ephemeral iron(III) and sulfide phases during redox cycles within contaminated floodplain soils. Env. Sci. Technol. 55 (9), 5878–5886.

Dewey, C., Fox, P.M., Bouskill, N.J., Dwivedi, D., Nico, P., Fendorf, S., 2022. Beaver dams overshadow climate extremes in controlling riparian hydrology and water quality. Nat. Commun. 13 (1), 6509.

Dia, A., Gruau, G., Olivié-Lauquet, G., Riou, C., Molénat, J., Curmi, P., 2000. The distribution of rare earth elements in groundwaters: assessing the role of source-rock composition, redox changes and colloidal particles. Geochim. Cosmochim. Acta 64 (24), 4131–4151.

Dibbern, D., Schmalwasser, A., Lueders, T., Totsche, K.U., 2014. Selective transport of plant root-associated bacterial populations in agricultural soils upon snowmelt. Soil Biol. Biochem. 69, 187–196.

Dong, H., Zeng, Q., Sheng, Y., Chen, C., Yu, G., Kappler, A., 2023. Coupled iron cycling and organic matter transformation across redox interfaces. Nat. Rev. Earth Environ. 4 (9), 659–673.

Dynes, J.J., Lawrence, J.R., Korber, D.R., Swerhone, G.D.W., Leppard, G.G., Hitchcock, A.P., 2006a. Quantitative mapping of chlorhexidine in natural river biofilms. Sci. Total Environ. 369 (1), 369–383.

Dynes, J.J., Regier, T.Z., Snape, I., Siciliano, S.D., Peak, D., 2015. Validating the scalability of soft X-ray spectromicroscopy for quantitative soil ecology and biogeochemistry research. Env. Sci. Technol. 49 (2), 1035–1042.

Dynes, J.J., Tyliszczak, T., Araki, T., Lawrence, J.R., Swerhone, G.D.W., Leppard, G.g., Hitchcock, A.P., 2006b. Speciation and quantitative mapping of metal species in microbial biofilms using scanning transmission X-ray microscopy. Env. Sci. Technol. 40, 1556–1565.

Engel, M., Noël, V., Pierce, S., Kovarik, L., Kukkadapu, R.K., Pacheco, J.S.L., Qafoku, O., Runyon, J.R., Chorover, J., Zhou, W., Cliff, J., Boye, K., Bargar, J.R., 2023. Structure and composition of natural ferrihydrite nano-colloids in anoxic groundwater. Water Res. 238, 119990.

Flury, M., Qiu, H., 2008. Modeling colloid-facilitated contaminant transport in the Vadose Zone. Vadose Zone J. 7 (2), 682–697.

Fox, P.M., Bill, M., Heckman, K., Conrad, M., Anderson, C., Keiluweit, M., Nico, P.S., 2020. Shale as a source of organic carbon in floodplain sediments of a mountainous watershed. J. Geophys. Res.: Biogeosciences 125 (2), e2019JG005419.

Giannetta, B., Oliveira de Souza, D., Aquilanti, G., Celi, L., Said-Pullicino, D., 2022. Redox-driven changes in organic C stabilization and Fe mineral transformations in temperate hydromorphic soils. Geoderma 406, 115532.

Harvey, J., Gooseff, M., 2015. River corridor science: hydrologic exchange and ecological consequences from bedforms to basins. Water Resour. Res. 51 (9), 6893–6922.

Hauer, F.R., Locke, H., Dreitz, V.J., Hebblewhite, M., Lowe, W.H., Muhlfeld, C.C., Nelson, C.R., Proctor, M.F., Rood, S.B., 2016. Gravel-bed river floodplains are the ecological nexus of glaciated mountain landscapes. Sci. Adv. 2 (6), e1600026.

Hitchcock, A.P., Ishii, I., 1987. Carbon K-shell excitation spectra of linear and branched alkanes. J. Electron Spectrosc. Relat. Phenom. 42 (1), 11–26.

Hitchcock, A.P., Urquhart, S.G., Rightor, E.G., 1992. Inner-shell spectroscopy of benzaldehyde, terephthalaldehyde, ethylbenzoate, terephthaloyl chloride and phosgene: models for core excitation of poly(ethylene terephthalate). J. Phys. Chem. 96 (22), 8736–8750.

Huang, W., Hammel, K.E., Hao, J., Thompson, A., Timokhin, V.I., Hall, S.J., 2019. Enrichment of lignin-derived carbon in mineral-associated soil organic matter. Env. Sci. Technol. 53 (13), 7522–7531.

Ishii, I., Hitchcock, A.P., 1988. The oscillator strengths for C1s and O1s excitation of some saturated and unsaturated organic alcohols, acids and esters. J. Electron Spectrosc. Relat. Phenom. 46 (1), 55–84.

Jin, Q., Bethke, C.M.and, 2007. The thermodynamics and kinetics of microbial metabolism. Am. J. Sci. 307 (4), 643–677.

Karunakaran, C., Christensen, C.R., Gaillard, C., Lahlali, R., Blair, L.M., Perumal, V., Miller, S.S., Hitchcock, A.P., 2015. Introduction of soft X-ray spectromicroscopy as an advanced technique for plant biopolymers research. PLoS One 10 (3), e0122959.

Käser, D., Hunkeler, D., 2016. Contribution of alluvial groundwater to the outflow of mountainous catchments. Water. Resour. Res. 52 (2), 680–697.

Keiluweit, M., Bougoure, J.J., Zeglin, L.H., Myrold, D.D., Weber, P.K., Pett-Ridge, J., Kleber, M., Nico, P.S., 2012. Nano-scale investigation of the association of microbial nitrogen residues with iron (hydr)oxides in a forest soil O-horizon. Geochim. Cosmochim. Acta 95, 213–226.

Keiluweit, M., Wanzek, T., Kleber, M., Nico, P., Fendorf, S., 2017. Anaerobic microsites have an unaccounted role in soil carbon stabilization. Nat. Commun. 8 (1), 1771.
Kogure, T., 2013. In: Bergaya, F., Lagaly, G. (Eds.), Developments in Clay Science. Elsevier, pp. 275–317.
Kretzschmar, R., Sticher, H., 1998. Colloid transport in natural porous media: influence of surface chemistry and flow velocity. Phys. Chem. Earth 23 (2), 133–139.
Lair, G.J., Zehetner, F., Fiebig, M., Gerzabek, M.H., van Gestel, C.A.M., Hein, T., Hohensinner, S., Hsu, P., Jones, K.C., Jordan, G., Koelmans, A.A., Poot, A., Slijkerman, D.M.E., Totsche, K.U., Bondar-Kunze, E., Barth, J.A.C., 2009. How do long-term development and periodical changes of river–floodplain systems affect the fate of contaminants? Results from European rivers. Environ. Pollut. 157 (12), 3336–3346.
Lehmann, K., Lehmann, R., Totsche, K.U., 2021. Event-driven dynamics of the total mobile inventory in undisturbed soil account for significant fluxes of particulate organic carbon. Sci. Total Environ. 756, 143774.
Liao, P., Pan, C., Ding, W., Li, W., Yuan, S., Fortner, J.D., Giammar, D.E., 2020. Formation and transport of Cr(III)-NOM-Fe colloids upon reaction of Cr(VI) with NOM-Fe(II) colloids at anoxic–Oxic interfaces. Env. Sci. Technol. 54 (7), 4256–4266.
Löv, Å., Cornelis, G., Larsbo, M., Persson, I., Sjöstedt, C., Gustafsson, J.P., Boye, K., Kleja, D.B., 2018. Particle- and colloid-facilitated Pb transport in four historically contaminated soils - speciation and effect of irrigation intensity. Appl. Geochem. 96, 327–338.
Lutfalla, S., Barré, P., Bernard, S., Le Guillou, C., Alléon, J., Chenu, C., 2019. Multidecadal persistence of organic matter in soils: multiscale investigations down to the submicron scale. Biogeosciences 16 (7), 1401–1410.
Lyvén, B., Hassellöv, M., Turner, D.R., Haraldsson, C., Andersson, K., 2003. Competition between iron- and carbon-based colloidal carriers for trace metals in a freshwater assessed using flow field-flow fractionation coupled to ICPMS. Geochim. Cosmochim. Acta 67 (20), 3791–3802.
Marcus, M.A., 2023. Data analysis in spectroscopic STXM. J. Electron Spectrosc. Relat. Phenom. 264, 147310.
Means, J.C., Wuayaratne, R., 1982. Role of natural colloids in the transport of hydrophobic pollutants. Science 215 (4535), 968–970.
Miller, M.P., Buto, S.G., Susong, D.D., Rumsey, C.A., 2016. The importance of base flow in sustaining surface water flow in the Upper Colorado River Basin. Water Resour. Res. 52 (5), 3547–3562.
Nierop, K.G.J.J., Jansen, B., Verstraten, J.M., 2002. Dissolved organic matter, aluminium and iron interactions: precipitation induced by metal/carbon ratio, pH and competition. Sci. Total Environ. 300 (1), 201–211.
Noël, V., Boye, K., Lezama Pacheco, J.S., Bone, S.E., Janot, N., Cardarelli, E., Williams, K. H., Bargar, J.R., 2017. Redox controls over the stability of U(IV) in floodplains of the Upper Colorado River Basin. Env. Sci. Technol. 51 (19), 10954–10964.
NOSAMS, 2023a. https://www2.whoi.edu/site/nosams/wp-content/uploads/sites/124/2023/02/GraphiteReductionMethod.pdf.
NOSAMS, 2023b. https://www2.whoi.edu/site/nosams/wp-content/uploads/sites/124/2023/02/OrganicCarbonMethod.pdf.
NOSAMS, 2023c. https://www2.whoi.edu/site/nosams/wp-content/uploads/sites/124/2023/02/SedimentPretreatmentMethod.pdf.
Opperman, J., Galloway, G. and Duvail, S. (2013) The multiple benefits of river–Floodplain connectivity for people and biodiversity, pp. 144–160.
Pan, S., Wu, P., Sun, L., Chen, M., Li, B., Wang, T., Shang, Z., Fang, J., Zhu, N., Dang, Z., 2024. The interaction between organic acids and green rust-Co(II): mineralogical changes of green rust and redistribution of Co(II). Environ. Pollut. 363, 125061.
Pédrot, M., Boudec, A.L., Davranche, M., Dia, A., Henin, O., 2011. How does organic matter constrain the nature, size and availability of Fe nanoparticles for biological reduction? J. Colloid Interface Sci. 359 (1), 75–85.
Pédrot, M., Dia, A., Davranche, M., Bouhnik-Le Coz, M., Henin, O., Gruau, G., 2008. Insights into colloid-mediated trace element release at the soil/water interface. J. Colloid Interface Sci. 325 (1), 187–197.
Perzan, Z., Babey, T., Caers, J., Bargar, J.R., Maher, K., 2021. Local and global sensitivity analysis of a reactive transport model simulating floodplain redox cycling. Water Resour. Res. 57 (12), e2021WR029723.
Pontoni, L., Van Hullebusch, E.D., Pechaud, Y., Fabbricino, M., Esposito, G., Pirozzi, F., 2016. Colloidal mobilization and fate of trace heavy metals in semi-saturated artificial soil (OECD) irrigated with treated wastewater. Sustainability 8 (12), 1257.
Prince, K.C., Avaldi, L., Coreno, M., Camilloni, R., Simone, M.d., 1999. Vibrational structure of core to Rydberg state excitations of carbon dioxide and dinitrogen oxide. J. Phys. B: At. Mol. Opt. Phys. 32 (11), 2551.
Rasmussen, A.N., Tolar, B.B., Bargar, J.R., Boye, K., Francis, C.A., 2024. Diverse and unconventional methanogens, methanotrophs, and methylotrophs in metagenome-assembled genomes from subsurface sediments of the Slate River floodplain, Crested Butte, CO, USA. mSystems. 9 (7), e00314–e00324.
Ravel, B., Newville, M., 2005. Athena, Artemis, Hephaestus: data analysis for X-ray absorption spectroscopy using IFEFFIT. J. Synchrotron. Radiat. 12, 537–541.
Riedel, T., Zak, D., Biester, H., Dittmar, T., 2013. Iron traps terrestrially derived dissolved organic matter at redox interfaces. Proc. Natl. Acad. Sci. 110 (25), 10101–10105.
Said-Pullicino, D., Giannetta, B., Demeglio, B., Missong, A., Gottselig, N., Romani, M., Bol, R., Klumpp, E., Celi, L., 2021. Redox-driven changes in water-dispersible colloids and their role in carbon cycling in hydromorphic soils. Geoderma 385, 114894.
Solomon, D., Lehmann, J., Harden, J., Wang, J., Kinyangi, J., Heymann, K., Karunakaran, C., Lu, Y., Wirick, S., Jacobsen, C., 2012. Micro- and nano-environments of carbon sequestration: multi-element STXM–NEXAFS spectromicroscopy assessment of microbial carbon and mineral associations. Chem. Geol. 329, 53–73.
Spielman-Sun, E., Boye, K., Dwivedi, D., Engel, M., Thompson, A., Kumar, N., Noël, V., 2024. A critical look at colloid generation, stability, and transport in redox-dynamic environments: challenges and perspectives. ACS Earth Space Chem. 8 (4), 630–653.
Stanford, J.A., Ward, J.V., 1993. An ecosystem perspective of alluvial rivers: connectivity and the Hyporheic corridor. J. North Am. Benthol. Soc. 12 (1), 48–60.
Stolze, L., Arora, B., Dwivedi, D., Steefel, C., Li, Z., Carrero, S., Gilbert, B., Nico, P., Bill, M., 2023. Aerobic respiration controls on shale weathering. Geochim. Cosmochim. Acta 340, 172–188.
ThomasArrigo, L.K., Kaegi, R., Kretzschmar, R., 2019. Ferrihydrite growth and transformation in the presence of ferrous iron and model organic ligands. Env. Sci. Technol. 53 (23), 13636–13647.
Thompson, A., Chadwick, O.A., Boman, S., Chorover, J., 2006. Colloid mobilization during soil iron redox oscillations. Env. Sci. Technol. 40 (18), 5743–5749.
Thompson, A., Rancourt, D.G., Chadwick, O.A., Chorover, J., 2011. Iron solid-phase differentiation along a redox gradient in basaltic soils. Geochim. Cosmochim. Acta 75 (1), 119–133.
Viviroli, D., Weingartner, R., 2004. The hydrological significance of mountains: from regional to global scale. Hydrol. Earth Syst. Sci. 8 (6), 1017–1030.
Vogel, J.S., Southon, J.R., Nelson, D.E., Brown, T.A., 1984. Performance of catalytically condensed carbon for use in accelerator mass spectrometry. Nucl. Instrum. Methods Phys. Res. B: Beam Interact. Mater. At. 5 (2), 289–293.
Wan, J., Tyliszczak, T., Tokunaga, T.K., 2007. Organic carbon distribution, speciation, and elemental correlations within soil micro aggregates: applications of STXM and NEXAFS spectroscopy. Geochim. Cosmochim. Acta 71 (22), 5439–5449.
Wang, C., Gomez-Velez, J.D., Wilson, J.L., 2018. The importance of capturing topographic features for modeling groundwater flow and transport in mountainous watersheds. Water Resour. Res. 54 (12), 10313-310338.
Ward, A.S., Schmadel, N.M., Wondzell, S.M., Harman, C., Gooseff, M.N., Singha, K., 2016. Hydrogeomorphic controls on hyporheic and riparian transport in two headwater mountain streams during base flow recession. Water Resour. Res. 52 (2), 1479–1497.
Watts, B., Finizio, S., Raabe, J., 2022. Quantifying signal quality in scanning transmission X-ray microscopy. J. Synchrotron. Radiat. 29 (4), 1054–1064.
Watts, B., Pilet, N., Sarafimov, B., Witte, K., Raabe, J., 2018. Controlling optics contamination at the PolLux STXM. J. Instrum. 13 (04), C04001.
Winkler, P., Kaiser, K., Thompson, A., Kalbitz, K., Fiedler, S., Jahn, R., 2018. Contrasting evolution of iron phase composition in soils exposed to redox fluctuations. Geochim. Cosmochim. Acta 235, 89–102.
Wohl, E., Lininger, K.B., Scott, D.N., 2018. River beads as a conceptual framework for building carbon storage and resilience to extreme climate events into river management. Biogeochemistry 141 (3), 365–383.
Xu, L., Roberts, M.L., Elder, K.L., Kurz, M.D., McNichol, A.P., Reddy, C.M., Ward, C.P., Hanke, U.M., 2021. Radiocarbon in dissolved organic carbon by UV oxidation: procedures and blank characterization at NOSAMS. Radiocarb 63 (1), 357–374.
Yu, P., Fu, F., Sun, G., Tang, B., 2021. Effects of oxalate and citrate on the behavior and redistribution of Cr(VI) during ferrihydrite-Cr(VI) co-precipitates transformation. Chemosphere 266, 128977.
Zhou, Z., Latta, D.E., Noor, N., Thompson, A., Borch, T., Scherer, M.M., 2018. Fe(II)-catalyzed transformation of organic matter-ferrihydrite coprecipitates: a closer look using Fe isotopes. Env. Sci. Technol. 52 (19), 11142–11150.